Constrained sintering of 8 mol % Y_2O_3 stabilised zirconia films

Xin Wang, Jung-Sik Kim[1], and Alan Atkinson[2]

Department of Materials, Imperial College, London SW7 2AZ, UK.

[1] Present address: Department of Aeronautical and Automotive Engineering, Loughborough University, Loughborough, LE11 3TU, UK.

[2] Corresponding author alan.atkinson@imperial.ac.uk, tel +44(0)2075946780

Abstract

The constrained sintering kinetics of 8 mol % Y_2O_3/92 mol % ZrO_2 (8YSZ) films approximately 10 - 15 μm thick screen-printed on dense YSZ substrates, and the resulting stress induced in the films, were measured in the temperature range 1100 to 1350°C. The results are compared with those reported earlier for yttria-partially stabilised zirconia (3YSZ) films.

Both materials behave similarly, although there are differences in detail. The constrained densification rate was greatly retarded compared with the unconstrained densification rate measured on pellets and free-standing films at a given temperature and density. The degree of retardation is too large to be explained by simple models of constrained sintering. This is due to the effect of the constraint on the developing anisotropic microstructure and, in the case of 8YSZ, considerable grain growth.

The stress generated during constrained sintering was measured by monitoring substrate bending in-situ during sintering and was typically a few MPa. This method also requires the substrate viscosity (creep) to be measured. The apparent activation energies for free sintering, constrained sintering, creep and grain growth are found to cover a wide range (135 – 670 kJ $mole^{-1}$) despite all probably being mainly controlled by grain boundary cation diffusion. The reasons for this are discussed and the dangers inherent in deducing

mechanisms of such complex phenomena from their apparent activation energies are highlighted.

Keywords sintering; films; ZrO_2; fuel cells; porosity.

1 Introduction

Many useful device structures involve sintering a layer of ceramic powder onto an effectively rigid substrate that constrains the shrinkage of the layer to one dimension. This is true for electrolytes in some designs of solid oxide fuel cell (SOFC) and also for the electrodes of SOFCs. In the case of the electrolyte the layer must sinter to high density in order to be gas impermeable and have high ionic conductivity, and this is inhibited by the constraint of the substrate.

Many planar SOFC concepts have a supported thick film electrolyte with typical thickness in the range 5 – 20 μm in order to reduce the ohmic resistance loss associated with the electrolyte. The electrolyte films are usually fabricated by sintering a green powder layer that has been deposited on a substrate by screen printing, or a related method. Currently the most common electrolyte materials are based on doped zirconia [1]. 8YSZ (8 mol % Y_2O_3 doped zirconia) has the cubic structure and a high ionic conductivity, and is favoured by most SOFC developers. 3YSZ (3 mol % Y_2O_3 doped zirconia), with the tetragonal structure, has a lower ionic conductivity, but better mechanical properties and is preferred for this reason by some developers [2].

Anode-supported SOFCs are usually fabricated by co-sintering the electrolyte and the anode support and any mismatch in the free sintering kinetics of the individual layers leads to stress and distortion during the sintering process [3]. However, because there is common shrinkage in the plane of the bi-layer, only partial constraint is applied to shrinkage of each individual layer by any mismatch in the free shrinkage rates. In other concepts (e.g. the integrated planar or segmented in series design of Rolls-Royce Fuel Cell Systems [4]) the substrate is effectively rigid. In such cases the electrolyte layer is fully constrained in its plane during sintering and shrinkage only occurs perpendicular to this plane (except within a distance of a few layer thicknesses of the layer edges).

Constrained sintering is also a feature of processing ceramic films on non-shrinking substrates for a wide range of other applications and is a topic of considerable fundamental interest. The constraint results in a tensile stress in the plane of the film that is just sufficient to oppose its tendency to shrink in this plane, were it not for the constraint, and this has two main consequences. The first is that the densification is retarded [5,6] in comparison with an unconstrained case, and the second is that the in-plane tensile stress can cause crack-like defects and porous channels in the constrained film, or delamination from the substrate [7,8]. In a related publications [9,10] we have reported measurements of the sintering-induced stress and sintering kinetics for 3YSZ screen-printed films constrained by 3YSZ substrates. In the current paper we report a similar study of the constrained sintering of 8YSZ films and compare the results with the earlier study of 3YSZ films.

2 Materials and methods

2.1 Specimens

The films and substrates were chosen to be the same composition to ensure that no stresses would be generated by thermal expansion differences between the film and substrate. The substrates for stress measurements were commercially produced by Kerafol GmbH (Eschenbach, Germany) and were received in the form of 5 x 5 cm square plates 115 and 150 μm in thickness. The grain size was measured by the linear intercept method to be 8.6 μm. The YSZ powders used to prepare the screen-printing inks and other specimens were supplied by MEL Chemicals, UK. The particle size distributions were measured by light scattering and the results are presented in Table 1. The two powders have similar median particle size, but the 8YSZ powder has a slightly wider size distribution.

For sintering dilatometry of the constrained films, thick substrates were prepared. YSZ powder compacts were produced by uniaxial die-pressing at 150 MPa and then sintered at

1400°C for 2 h to give discs 36 mm diameter and 0.7 mm thickness. The surfaces of the discs were ground flat and parallel and then one face was polished to 1 μm diamond finish to receive the screen printed film. YSZ layers were deposited on the substrates by screen printing (165 mesh screen and 2.5 mm gap) and the layers were oven dried at 120 °C. At this stage the films were in the thickness range 10-15 μm.

Cylindrical specimens (approximate dimensions 6 mm diameter x 5 mm length) were prepared for conventional dilatometry by die pressing dry powders at 150 MPa followed by isostatic pressing at 300MPa. Free-standing "film" specimens were also prepared from the screen printing ink by tape casting the ink onto Mylar sheet substrates and removing them after drying.

2.2 Sintering kinetics

Conventional dilatometry to measure unconstrained sintering was carried out in a push-rod dilatometer (Netzsch DIL 402 E). Different controlled heating rates (3-30 K min^{-1}) were used in order to obtain the apparent activation energy for unconstrained densification. The final density was calculated from the mass of the specimen and its final dimensions.

Constrained sintering of screen printed films was measured using an optical dilatometer and the details have been described previously [10]. The displacement data over the whole of an experimental run were calibrated against the actual film thickness change measured before and after sintering using an interference microscope (ZYGO NewView, Middlefield, USA). The final densities of films sintered at the higher temperatures were estimated from image analysis of SEM images of their final structure and their final film thickness was also confirmed by SEM to be consistent with the interference microscope measurements. The film green density was then calculated from the final density and the measured change in film thickness.

The sintering kinetics of unconstrained films were measured on fragments of green films,

removed after being tape cast onto Mylar substrates, using optical image analysis as described in [10].

2.3 Sintering-induced stress

The method used for measuring sintering-induced stress is based on monitoring *in situ* the deformation during sintering of a vertical coated strip specimen after measuring the creep viscosity of the uncoated substrate in a similar horizontal cantilever beam configuration. The details of the experiments and method of analysis have been described previously [9].

3 Results

3.1 Unconstrained sintering

Figure 1 shows the linear shrinkage rate curves of bulk specimens (free sintering) at a constant heating rate of 20 K min^{-1}. The curves for 8YSZ and 3YSZ differ mainly in that 8YSZ shows a stronger reduction in densification rate than 3YSZ at the higher temperatures and densities. The apparent activation energy for free sintering of 8YSZ was calculated in two ways as described previously for 3YSZ [10]. The first is from Arrhenius plots of densification rate at constant density and the second by fitting to a master sintering curve [11]. Figure 2 shows the master sintering curve for 8YSZ in which the relative density is plotted as a function of the parameter Θ defined as:

$$\Theta(t,T) = \int_0^t \frac{1}{T} exp\left(\frac{-Q_s}{RT}\right) dt \qquad (1)$$

where Q_s is the activation energy for sintering and in this plot is 650 kJ mol^{-1}. The average activation energy for unconstrained sintering was 670 ± 30 kJ mol^{-1} and is the same as determined previously for 3YSZ (Table 2) to within experimental error.

3.2 Constrained sintering

The densification of the constrained films at a heating rate of 20 K min^{-1} is compared with those of unconstrained bulk specimens at the same heating rate in Figure 3. The large degree of retardation caused by the constraint is evident for both compositions even though the screen printed films have higher green density than the isostatically pressed compacts. Also shown is the densification of the free-standing film tape-cast from the screen printing ink. The densification of the unconstrained film is consistent with that of the bulk specimen given the higher green density of the film.

In order to study the retardation in greater detail the densification kinetics were studied under isothermal conditions. The isothermal densification kinetics (after heating to the isothermal temperature at 20 K min^{-1}) for the constrained films are shown in Figure 4. Both 3YSZ and 8YSZ exhibit similar behaviour. It was not possible to compare the experimental data for isothermal densification kinetics of both constrained and free specimens directly because there was insufficient overlap of density at a given temperature. Therefore the isothermal kinetics for free sintering were calculated using the master sintering curve. In addition the raw data for constrained sintering (Figure 4) have considerable noise and therefore were smoothed by fitting to polynomials (of order 4 to 6).

The resulting densification curves, were then differentiated and the relative rates of constrained and free densification were calculated at different densities. The result is shown in Figure 5 compared with the results obtained previously for 3YSZ using the same approach [10]. There is a clear trend for the retardation caused by the constraint to become larger as both the temperature and density increase. However, it is not clear which of these is controlling as they are strongly correlated. Both compositions behave very similarly, although the retardation is stronger for 3YSZ, particularly at lower densities.

Figure 6 shows an Arrhenius plot of the constrained densification rates for 8YSZ at two

different relative densities. The range of densities is quite narrow because there is limited overlap for a suitable range of temperature. The average apparent activation energy is approximately 190 ± 20 kJ mol^{-1} which is similar to that reported previously for 3YSZ (Table 2) and much lower than for free sintering. The reason for this much lower apparent activation energy is that the retardation caused by the constraint increases with increasing temperature as seen in Figure 5.

3.3 Sintering-induced stress

Figure 7 shows the typical time variation of displacement at the tip of a thin horizontal beam dense 8YSZ substrate specimen undergoing creep driven by gravity. The displacement increases approximately linearly with time, although there is a slight downward curvature as reported previously for 3YSZ beams [9]. The creep viscosity of the 8YSZ thin substrates was calculated from the average rate of tip deflection over the observation period and the results are shown in the Arrhenius plot in Figure 8. The viscosity is much higher than for the 3YSZ substrates but the apparent activation energy of 330 ± 20 kJ mol^{-1} is the same to within experimental error.

Also shown in Figure 7 is an example of bending of a vertical cantilever beam caused by the sintering induced stress in a film applied to one side of the beam. The average rate of tip deflection was used to calculate the stress in the film as described previously [9] and the results obtained at different temperatures are presented in Figure 9 compared with the earlier results for 3YSZ films. Because of the high substrate viscosity for 8YSZ, it was not possible to measure the sintering induced stress reliably at temperatures below 1200°C, even using the thinnest (115 μm) substrates, and the error bars are larger than for 3YSZ even at higher temperatures. The sintering induced stress is higher for 8YSZ than for 3YSZ and particularly so at 1350°C.

4 Discussion

4.1 Unconstrained densification kinetics

The dependence of unconstrained sintering rate on temperature and density for 8YSZ is seen in Figure 1 is qualitatively different from that of 3YSZ at high density and temperature. This is also evident in Figure 2, where the master sintering curve for 8YSZ is not fitted well at high densities. The reason for this is the much faster grain growth in 8YSZ compared with 3YSZ. This phenomenon has been reported extensively in the literature. Matsui et al. [12] concluded that grain boundary mobility in YSZ was controlled by solute drag and that this was lower in 8YSZ (faster grain growth) because the degree of Y segregation to the grain boundaries is smaller than in 3YSZ.

In an earlier study, we reported grain size measured as a function of time, temperature and relative density during unconstrained sintering by the linear intercept method on polished and etched cross sections of 3YSZ and 8YSZ. Some of the results are presented in Figure 7 of reference [13] and clearly show that 8YSZ undergoes much more grain growth during sintering. Grain growth for both 3YSZ and 8YSZ was fitted to a "master grain growth" kinetic equation

$$G_t^m - G_o^m = m\int_0^t k_o \, exp\left(-\frac{Q_G}{RT}\right)dt \qquad (2)$$

(where G is the grain size, the exponent m is typically between 2 and 4, and Q_G is the activation energy for grain growth) and the resulting parameters are given in Table 3 [13]. The activation energies for grain growth are the same for the two materials to within experimental error, which is consistent with the mechanism being solute drag in both cases. However, the exponent, m, is very different for the two materials; the lower value of m for 8YSZ is associated with its much faster grain growth.

Unconstrained sintering of 8YSZ has been studied in several recent works. Matsui et al. [14]

observed similar densification curves to those shown in Figure 1. They fitted isothermal initial densification kinetics (expressed as specimen dimension) to the equation

$$\frac{L-L_0}{L_0}=\left(\frac{K\gamma\Omega D}{kTa^p}\right)^n\left(t-t_0\right)^n \tag{3}$$

in which a is particle radius, γ surface energy, Ω atomic volume and K a numerical factor. D is the diffusion coefficient for the rate controlling transport process. They found n to be 1/3 for both 3YSZ and 8YSZ, which they interpret as indicating grain boundary diffusion to be rate controlling, and the activation energies were 670 kJ mol^{-1} for 3YSZ and 757 kJ mol^{-1} for 8YSZ. Suárez et al. [15] applied a similar analysis to their isothermal densification kinetics of 8YSZ. They report an activation energy of 170 kJ mol^{-1} for the densification kinetics, but their definition of the rate constant is different from Equation 3 by the power of n. Thus to compare the activation energies for diffusion the activation energy of Suárez et al. should be divided by n (which they found to be 0.30 ± 0.05) and leads to an activation energy of 570 kJ mol^{-1}. Finally Suárez and Sakka [16] analysed constant heating rate experiments similar to the ones in the present study, and found an activation energy of 716 kJ mol^{-1}. Thus the activation energies for unconstrained sintering in the present study (Table 2) are consistent with activation energies for unconstrained sintering reported in the literature.

4.2 Constrained densification kinetics

Assuming isotropic linear viscous properties for the sintering body, the relationship between the densification rate for a constrained film, $\dot{\rho}_{constr}$, and the unconstrained material, $\dot{\rho}_{free}$, is given by [17,18]

$$\frac{\dot{\rho}_{constr}}{\dot{\rho}_{free}}=\frac{\left(1+\nu_p\right)}{3\left(1-\nu_p\right)} \tag{4}$$

where ν_p is the viscous Poisson's ratio. Since the minimum physically acceptable value for ν_p is 0, the lower bound of the constrained densification rate, based on this model, is 1/3 the

unconstrained rate (i.e. the strain rate perpendicular to the film plane is equal to the unconstrained strain rate). The results in Figure 5 for 3YSZ cannot be accounted for by this model, and, for 8YSZ, only in the initial stage are the constrained densification rates potentially explicable by this model. This behaviour is consistent with observations reported in the literature for alumina films [5,19] and is caused by the microstructure of the constrained film being different from the unconstrained body at the same relative density. The microstructure can differ in two major ways: first it can be coarser (in terms of grain size, pore size and inter-pore spacing); and second it can be anisotropic (in terms of the elongation and preferred orientation of pores and grains).

Bordia and Guillon [20,21] modified the isotropic viscous model to anisotropic viscous behaviour and applied it successfully to sinter-forging of alumina compacts. However, the theory is difficult to apply to constrained films because it requires two independently measured (or modelled) free strain rates and two viscous Poisson's ratios corresponding to in-plane and out-of-plane principal directions. Li et al. [22] also developed a theory of constrained sintering based upon anisotropic constitutive viscous deformation equations. In order to circumvent the requirement for data explicitly describing the anisotropic properties as a function of density, they proposed a simplified version with only a single adjustable parameter. This was applied in our previous study of 3YSZ and the result for the predicted retardation is shown again in Figure 5. It is clear that this theory does not reproduce the trend with relative density seen in the present experiments and moreover it predicts that the apparent activation energies for constrained and free sintering are equal, which we do not observe in the experiments on both 3YSZ and 8YSZ. Hence it is concluded that the microstructure in constrained sintering of these materials develops in ways that are not captured by the isotropic viscous theory or the simplified version of the theory of Li et al.

Since grain growth is not influenced significantly by the sintering induced stress, there is

more grain growth in constrained sintering (to reach a given density) than in unconstrained sintering because the slower constrained densification kinetics allow more time for grain growth to take place. The data in Figure 3 show that the unconstrained film reaches a relative density of 75% at 1250°C at which point the grain size is 0.24 μm. However, the constrained film requires an extra hold of 1 h at 1250°C to reach 75% density (Figure 4), by which time its grain size has increased to 0.39 μm. Assuming that the densification rate is proportional to G^{-4}, we estimated the ratio of constrained to free densification rates (retardation) to be 0.14 (14%). Similarly the unconstrained film reaches 80% density at 1300°C (Figure 3) whereas the constrained film again requires an additional 1 h at that temperature (Figure 4) during which the grain size increases from 0.39 to 0.79 μm. The corresponding retardation as a result of this grain growth is predicted to be 0.06 (6%). Thus the experimental retardation shown in Figure 5 can be accounted for semi-quantitatively in terms of grain growth. This is different from the situation for 3YSZ, where the much lower rates of grain growth could not fully account for the observed retardation [10].

It is now well-established that constrained sintering leads to anisotropy and heterogeneity in the microstructure and we previously argued that this made a major contribution to the retardation of densification of 3YSZ films during constrained sintering [10]. However, in the case of 8YSZ the anisotropy in the microstructure is significantly lower [13]. This is reflected in (for 8YSZ): smaller average pore size at a given density; more isotropic pore shape; and lower degree of preferred pore orientation with respect to film thickness direction. From the microstructure evolution model, these observations are probably the result of a higher ratio of surface to grain boundary diffusion coefficients in 8YSZ [13].

4.3 Creep

The creep viscosity of the 8YSZ beams used in the present study is compared with the earlier similar measurements on 3YSZ reported previously [9]. The viscosity of 8YSZ is

significantly larger than for 3YSZ. For creep controlled by grain boundary diffusion (Coble creep) the viscosity is proportional to the grain size cubed, and for control by lattice diffusion (Nabarro-Herring creep) to the grain size squared. Chokshi [23] has discussed creep in 3YSZ and 8YSZ in terms of reported diffusion coefficients using the following relationships.

$$E_p = \frac{kT}{28 D_L b}\left(\frac{G}{b}\right)^2 \quad \text{for Nabarro-Herring creep, and} \tag{5}$$

$$E_p = \frac{kT}{33 D_{gb} \delta}\left(\frac{G}{b}\right)^3 \quad \text{for Coble creep} \tag{6}$$

In these expressions b is the magnitude of the Burgers vector, D_L the lattice diffusion coefficient, D_{gb} the grain boundary diffusion coefficient and δ the boundary width. Sudhir and Chokshi [24] have reported compression creep data for 8YSZ with a grain size of 5 μm and their measurements have been adjusted to the current grain size of 8.6 μm assuming Coble creep (as concluded by Sudhir and Chokshi). The result is compared with the present data in Figure 8. The two sets of experiments are in reasonable agreement although the activation energy in the present study (280 kJ mol^{-1}) is somewhat lower than that reported by Sudhir and Chokshi (430 kJ mol^{-1}).

The larger grain size of the 8YSZ beams (8.6 μm) compared to those of 3YSZ used previously (0.46 μm) is expected to result in higher creep viscosity for 8YSZ as is observed in Figure 8. The ratio of grain sizes is 8.6/0.46 = 18.7 and the ratio of viscosities would be expected to be 350 for Nabarro-Herring creep and 6500 for Coble creep. However the observed ratio is only approximately 200. This implies either that grain boundary diffusion of the rate-controlling cation (probably Zr^{4+}) is larger in 8YSZ than 3YSZ, or other processes are influencing the deformation rate.

Substituting independently measured diffusion data into Equations 5 and 6, Chokshi [23] concluded that Nabarro-Herring creep would only be dominant in 3YSZ or 8YSZ ceramics

having grain sizes orders of magnitude larger than found in typical ceramics. At 1300°C the grain boundary diffusion coefficients quoted by Chokshi are approximately an order of magnitude higher for 8YSZ than 3YSZ which could explain their relative creep viscosities measured in the present work. The activation energies for grain boundary diffusion quoted by Chokshi are 309 kJ mole^{-1} for 8YSZ and 506 kJ mole^{-1} for 3YSZ, whereas the creep activation energies in the current work are approximately the same for both materials. However, Swaroop et al. [25] report an activation energy of 370 ± 30 kJ mole^{-1} for Hf grain boundary diffusion in 3YSZ. Therefore the activation energies for grain boundary diffusion in 3YSZ and 8YSZ are not too different.

4.4 Stress induced by constrained sintering

Assuming linear viscous deformation of the film, and isotropic microstructure, the sintering-induced stress for a constrained film is given by [26]

$$\sigma = \frac{E_{p,f}\dot{\varepsilon}_f}{1-\nu_{p,f}} \tag{7}$$

where $\dot{\varepsilon}_f$ is the unconstrained sintering rate and $E_{p,f}$ and $\nu_{p,f}$ are the viscosity and Poisson's ratio of the film. This relationship is not strictly applicable in the present case, because the microstructure is known to be anisotropic. Nevertheless, it provides a basis for qualitative interpretation of the observations. The key difference between the behaviour of 3YSZ and 8YSZ seen in Figure 9 is the much higher induced stress in 8YSZ at the higher temperatures (which also correspond to higher densities). It has been noted in the preceding discussion that the main microstructural difference between 3YSZ and 8YSZ is the much greater grain growth in 8YSZ. This influences both $\dot{\varepsilon}_f$ and E_{pf}, but in opposite ways. The appropriate unconstrained densification rate is that at the same microstructure and density of the constrained film. From the earlier discussion of densification kinetics it is clear that both the constrained and unconstrained densification rates are relatively insensitive to Y content and

therefore cannot explain a difference in induced stress according to Equation 7. However, the faster grain growth in 8YSZ will lead to a much higher creep viscosity at the higher temperatures than for 3YSZ and, from Equation 7, a higher induced stress. Therefore the qualitative difference between the two materials seen in Figure 9 is most probably due to the faster grain growth in 8YSZ.

4.5 Activation energies

All the apparent activation energies for the processes considered here are summarised in Table 2. They cover an extremely wide range despite the fact that all the processes are probably controlled by cation grain boundary diffusion, which diffusion studies suggest has an activation energy of approximately 370 kJ $mole^{-1}$ [25]. It is also evident that the main variability in the apparent activation energies comes from the process being considered and not from the material composition. It is therefore appropriate to consider the possible reasons for this variation.

For unconstrained sintering the activation energy is much higher than expected. This is probably because transport pathways other than grain boundary diffusion are operative. In particular, surface diffusion is expected to have lower activation energy than grain boundary diffusion and so would be favoured at the lower temperatures. However, surface diffusion does not result in densification, but it does remove some of the driving force for densification. This would result in a lowering of the densification rate, particularly at the lower temperatures and thereby a high apparent activation energy for densification.

Conversely, the apparent activation energy for constrained sintering is much lower than expected. As discussed earlier, this is due to the densification rate being preferentially retarded at the higher temperatures by anisotropy in the microstructure (3YSZ) and grain growth (8YSZ). This retardation lowers the apparent activation energy.

In the case of creep, the apparent activation energy is slightly lower than that of grain

boundary diffusion and this could be either due to a minor contribution from a faster process in parallel at low temperatures (such as grain boundary sliding) or a slower process in series at higher temperatures (such as availability of point defect sources and sinks in grain boundaries). It is also clear from the present experiments (Figure 7) that there is some small time dependence to the creep rate in these particular materials that is not explained by simple Coble creep.

The activation energies measured for grain growth are closest to the value for cation diffusion along grain boundaries. However, this is probably fortuitous, because grain growth involves atoms moving across the boundaries rather than along them and, furthermore, grain growth in YSZ is complicated by solute drag.

In summary, we observe a wide range of apparent activation energies for these processes despite the likelihood that they are all mainly controlled by diffusion of cations in the grain boundaries. The converse of this is that it is very dangerous to attempt to identify the rate controlling steps of such complex phenomena purely from their apparent activation energies.

5 Conclusions

The unconstrained and constrained sintering characteristics of 8YSZ are very similar to those reported previously for 3YSZ, although there are differences in detail. The main microstructural difference between the two compositions is the much greater grain growth of 8YSZ which influences both sintering and creep.

The constrained densification rate of both 3YSZ and 8YSZ was greatly retarded compared with the corresponding unconstrained densification rate at a given temperature and density. In both materials the degree of retardation is too large to be explained by simple models of constrained sintering. In 3YSZ this is mainly due to the constraint leading to an anisotropic microstructure whereas, in the case of 8YSZ, the retardation is mainly due to enhanced grain growth.

The creep viscosity of the dense 8YSZ substrates was much greater than that of 3YSZ substrates. Although this is expected from the larger grain size in the 8YSZ substrates, the increase in viscosity is less than predicted by simple Coble creep. This is probably due to grain boundary diffusion of cations in 3YSZ being faster than in 8YSZ at the temperatures studied.

The stress generated during constrained sintering was typically a few MPa in both materials. However, the stress in 8YSZ at high temperatures and densities was larger than in 3YSZ and this is probably due to the larger creep viscosity of 8YSZ.

The apparent activation energies for free sintering, constrained sintering, creep and grain growth are found to cover a wide range (135 – 670 kJ $mole^{-1}$) despite all probably being mainly controlled by grain boundary cation diffusion. This shows that it is not possible to deduce mechanisms of such complex phenomena purely from their apparent activation energies.

Acknowledgements

This research was carried out as part of the UK Supergen consortium project on "Fuel Cells: Powering a Greener Future". The Energy Programme is an RCUK cross-council initiative led by EPSRC and contributed to by ESRC, NERC, BBSRC and STFC.

References

1 Kharton VV, Marques FMB, Atkinson A. Transport properties of solid oxide electrolyte ceramics: a brief review. Solid State Ionics 2004;174:135-149.

2 Malzbender J, Steinbrech RW. Fracture test of thin sheet electrolytes for solid oxide fuel cells. J. Eur. Ceram. Soc. 2007;27: 2597-2603.

3 Steinbrech RW, Caron A, Blass G, Dias F. Influence of sintering characteristics on component curvature of electrolyte-coated anode substrates. In: Stimming U, Singhal

SC, Tagawa H, Lehnert W, editors. Proceedings of SOFC V, Electrochemical Society 1997 p. 727-736.

4 Costamagna P, Selimovic A, Del Borghi M, Agnew G. Electrochemical model of the integrated planar solid oxide fuel cell (IP-SOFC). Chemical Engineering Journal 2004;102:61-69.

5 Garino TJ, Bowen HK. Kinetics of constrained-film sintering. J. Am. Ceram. Soc. 1990;73:251-257.

6 Zhao Y, Dharani LR. Theoretical-model for the analysis of a ceramic thin-film sintering on a non-sintering substrate. Thin Solid Films 1994;245:109-114.

7 Jagota A, Hui CY. Mechanics of sintering thin-films 2: Cracking due to self-stress. Mechanics of Materials 1991;11:221-234.

8 Bordia RK, Jagota A. Crack-growth and damage in constrained sintering films. J. Am. Ceram. Soc. 1993;76:2475-2485.

9 Atkinson A, Kim J-S, Rudkin RA, Taub S, Wang X. Stress induced by constrained sintering of 3YSZ films measured by substrate creep. J. Am. Ceram. Soc. 2010; no. doi: 10.1111/j.1551-2916.2010.04160.x

10 “Constrained sintering kinetics of 3YSZ films”, Jung-Sik Kim, Robert A. Rudkin, Xin Wang, Alan Atkinson, Journal of the European Ceramic Society 31 (2011) 2231–2239.

11 Su H, Johnson DL. Master sintering curve: A practical approach to sintering. J. Am. Ceram. Soc. 1996;79:3211-3217.

12 K. Matsui, H. Yoshida and Y. Ikuhara, "Grain-boundary structure and microstructure development mechanism in 2-8 mol% yttria-stabilized zirconia polycrystals", Acta Materialia, 56 [6] 1315-1325 (2008).

13 Wang X, Atkinson A. Microstructure evolution in thin zirconia films: Experimental observation and modelling, Acta Materialia 2011; 59:2514-2525.

14 K. Matsui, K. Tanaka, T. Yamakawa, M. Uehara, N. Enomoto and J. Hojo, "Sintering kinetics at isothermal shrinkage: Ii, effect of y₂o₃ concentration on the initial sintering stage of fine zirconia powder", J. Am. Ceram. Soc., 90 [2] 443-447 (2007)

15 G. Suárez, L. B. Garrido and E. F. Aglietti, "Sintering kinetics of 8Y-cubic zirconia: Cation diffusion coefficient", Materials Chemistry and Physics, 110 [2â€“3] 370-375 (2008)

16 G. Suárez and Y. Sakka, "Effect of alumina addition on initial sintering of cubic zro2 (8ysz)", Ceramics International, 36 [3] 879-885 (2010)

17 Bordia RK, Scherer GW. Constrained sintering-I, constitutive model for a sintering body. Acta metallurgica 1988;36:2393-2298.

18 Bordia RK, Scherer GW. On constrained sintering-II, Comparison of constitutive models. Acta Metallurgica 1988;36:2399-2409.

19 Guillon O, Aulbach E, Rodel J, Bordia RK. Constrained sintering of alumina thin films: Comparison between experiment and modelling. J. Am. Ceram. Soc. 2007;90:1733-1737.

20 Bordia RK, Zuo R, Guillon O, Salamone SM, Rödel J. Anisotropic constitutive laws for sintering bodies. Acta Materialia 2006;54:111-118.

21 Guillon O, Nettleship I, Microstructural characterization of alumina films during constrained sintering, J. Am. Ceram. Soc. 2010; 93: 627-629.

22 Li F, Pan J, Guillon O, Cocks A. Predicting sintering deformation of ceramic film constrained by rigid substrate using anisotropic constitutive law. Acta Materialia 2010;58:5980-5988.

23 A. H. Chokshi, "Diffusion, diffusion creep and grain growth characteristics of nanocrystalline and fine-grained monoclinic, tetragonal and cubic zirconia", Scripta Materialia, 48 [6] 791-796 (2003)

24 B. Sudhir and A. H. Chokshi, "Compression creep characteristics of 8-mol%-yttria-stabilized cubic-zirconia", J. Am. Ceram. Soc., 84 [11] 2625-2632 (2001)

25 S. Swaroop, M. Kilo, C. Argirusis, G. n. Borchardt and A. H. Chokshi, "Lattice and grain boundary diffusion of cations in 3ytz analyzed using sims", Acta Mater., 53 [19] 4975-4985 (2005)

26 R.K Bordia and R. Raj, “Sintering behavior of ceramic films constrained by a rigid substrate”, J. Am. Ceram. Soc., 68 [6] 287-292 (1985).

Tables

Table 1 Particle size analysis

	3YSZ	**8YSZ**
d_{10} (μm)	0.38	0.13
d_{50} (μm)	0.50	0.44
d_{90} (μm)	0.77	1.87
SSA (m^2 g^{-1})	6.9	-

Table 2 Apparent activation energies (kJ mol^{-1})

Process	**3YSZ**	**8YSZ**
Free sintering	660 ± 20	670 ± 30
Constrained sintering	135 ± 20	190 ± 20
Creep	230 ± 20	280 ± 40
Grain growth	327 ± 30	331 ± 45

Table 3 Grain growth parameters

Material	m	k_o (μm^m s^{-1})	G_o (μm)	Q_G (kJ mol^{-1})
3YSZ	4	1.81×10^4	0.17	327 ± 30
8YSZ	2	2.86×10^6	0.15	331 ± 45

Figure captions

Figure 1 Free sintering densification rate in constant heating rate dilatometry (rate?) as a function of a) density and b) temperature.

Figure 2 Master sintering curve for bulk free sintering of 8YSZ plotted for 4 different heating rates and assuming an activation energy of 650 kJ mol^{-1}.

Figure 3 Constant heating rate (20 K min^{-1}) sintering curves comparing constrained and unconstrained specimens of 8YSZ with 3YSZ.

Figure 4 Isothermal densification kinetics of constrained films. 8YSZ kinetics shown as continuous lines and 3YSZ kinetics as broken lines.

Figure 5 The ratio of constrained to free densification rates as a function of density at different isothermal temperatures for 8YSZ (closed symbols) and 3YSZ (open symbols).

Figure 6 Arrhenius plot of the constrained densification rates at two different densities.

Figure 7 Example of bending of 8YSZ substrate cantilever beams at 1350°C in horizontal (no film) and vertical (with film on one side) orientations. The beam dimensions are 40 mm length by 150 μm thickness.

Figure 8 Creep viscosity of dense 3YSZ and 8YSZ substrates used to measure sintering induced stress.

Figure 9 Stress induced during constrained sintering of 3YSZ and 8YSZ films.

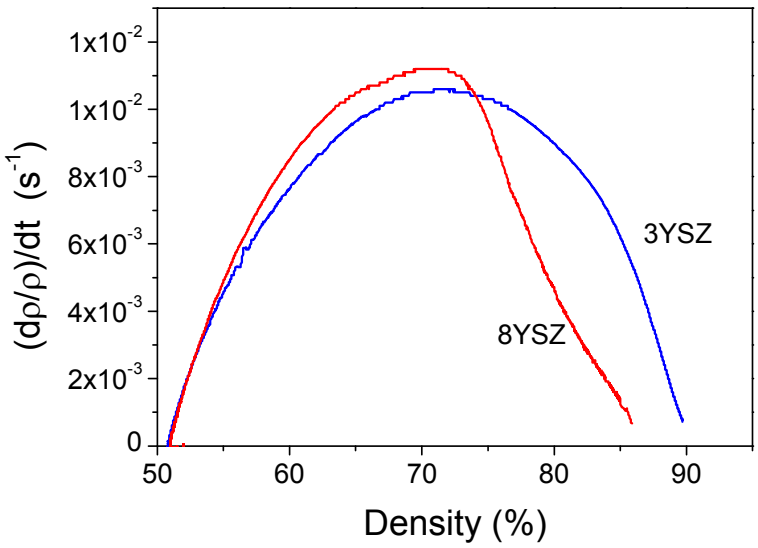

a)

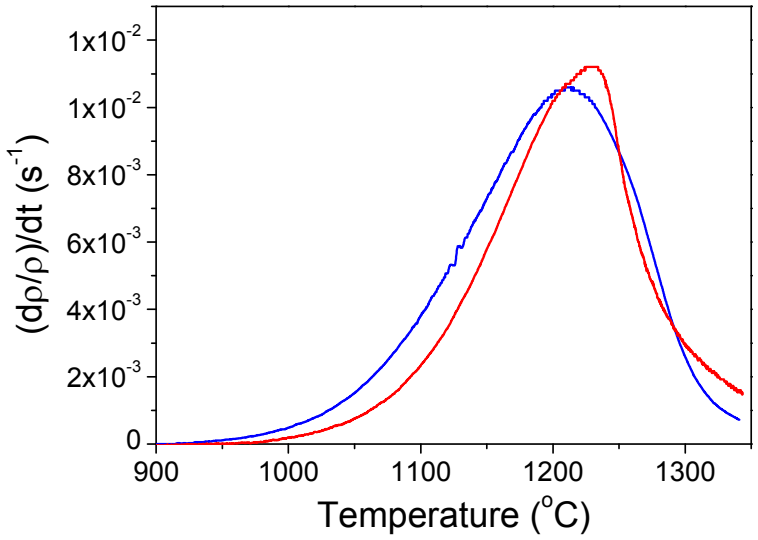

b)

Figure 1 Free sintering densification rate in constant heating rate dilatometry (rate?) as a function of a) density and b) temperature.

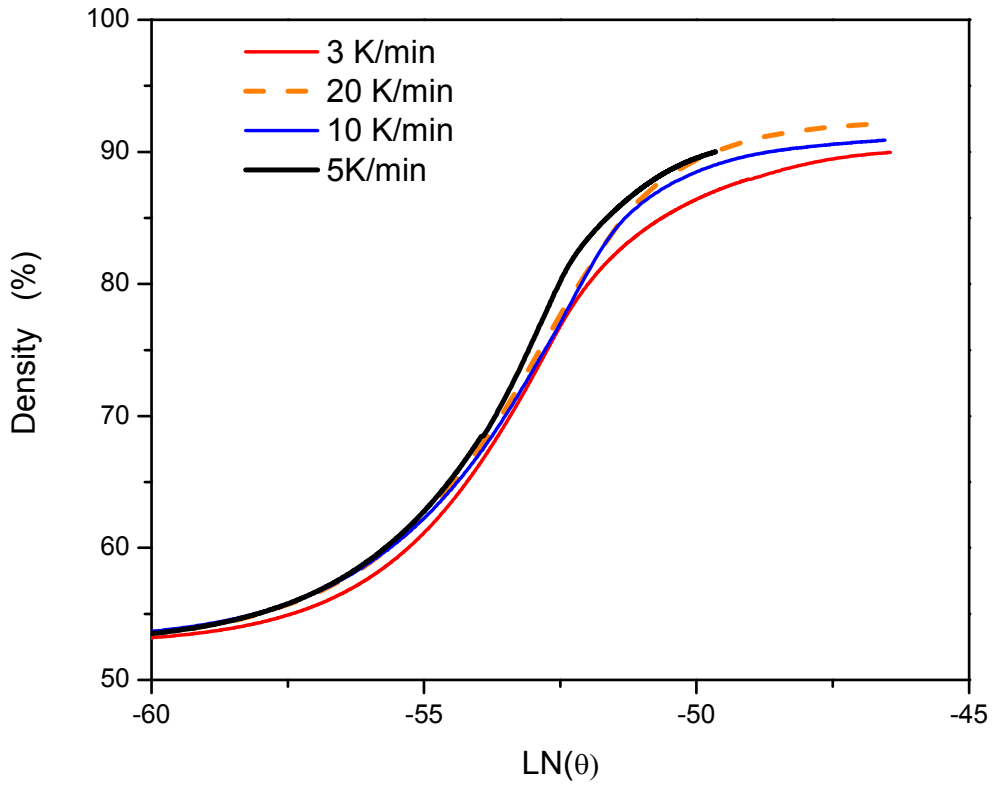

Figure 2 Master sintering curve for bulk free sintering of 8YSZ plotted for 4 different heating rates and assuming an activation energy of 650 kJ mol^{-1}.

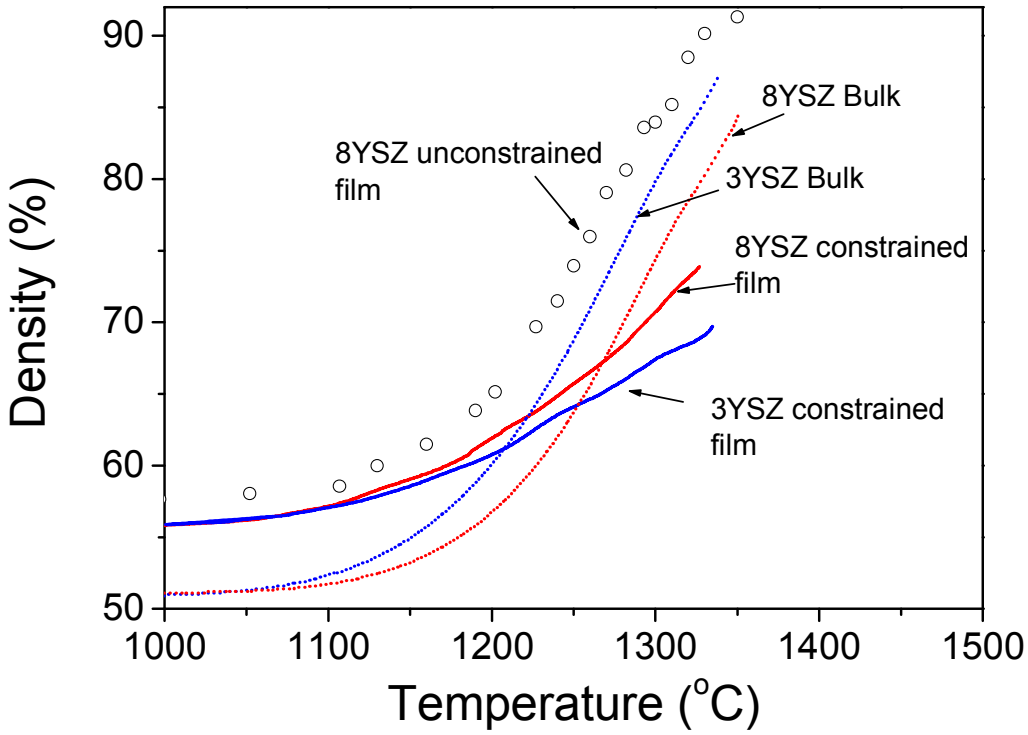

Figure 3 Constant heating rate (20 K min^{-1}) sintering curves comparing constrained and unconstrained densification of 8YSZ with 3YSZ.

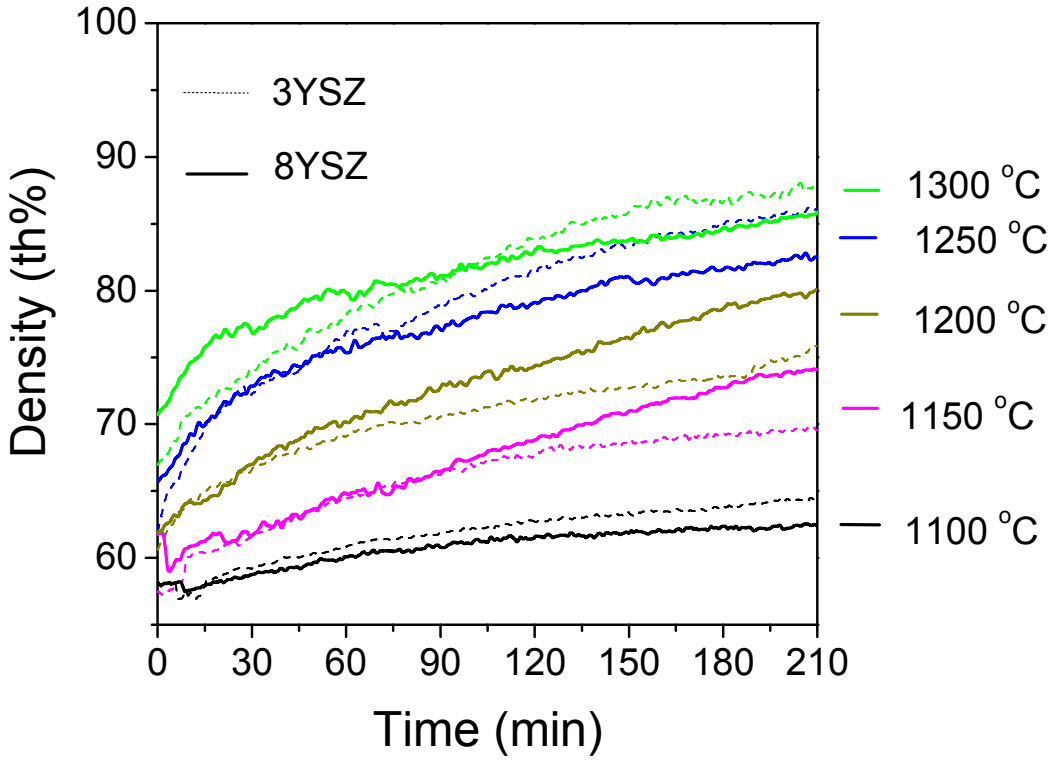

Figure 4 Isothermal densification kinetics of constrained films. 8YSZ kinetics shown as continuous lines and 3YSZ kinetics as broken lines.

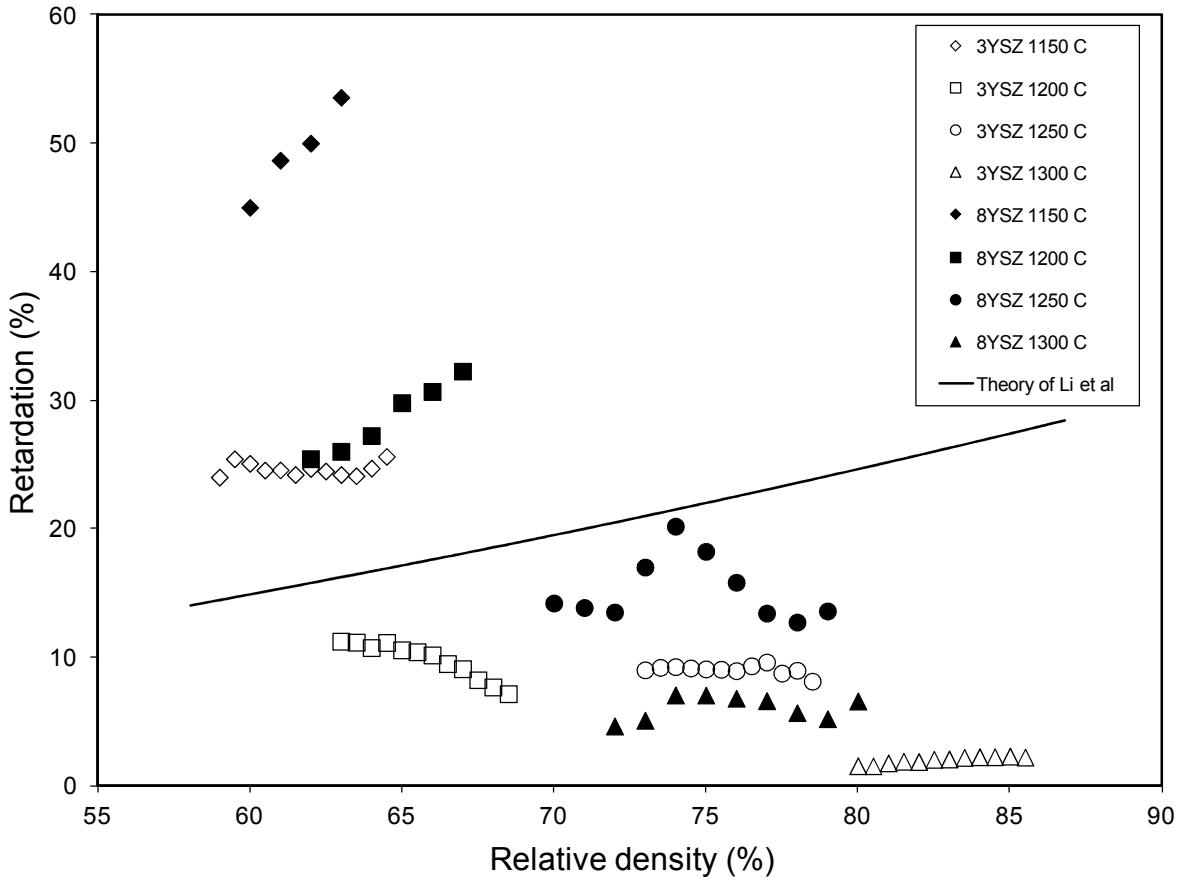

Figure 5 The ratio of constrained to free densification rates as a function of density at different isothermal temperatures for 8YSZ (closed symbols) and 3YSZ (open symbols).

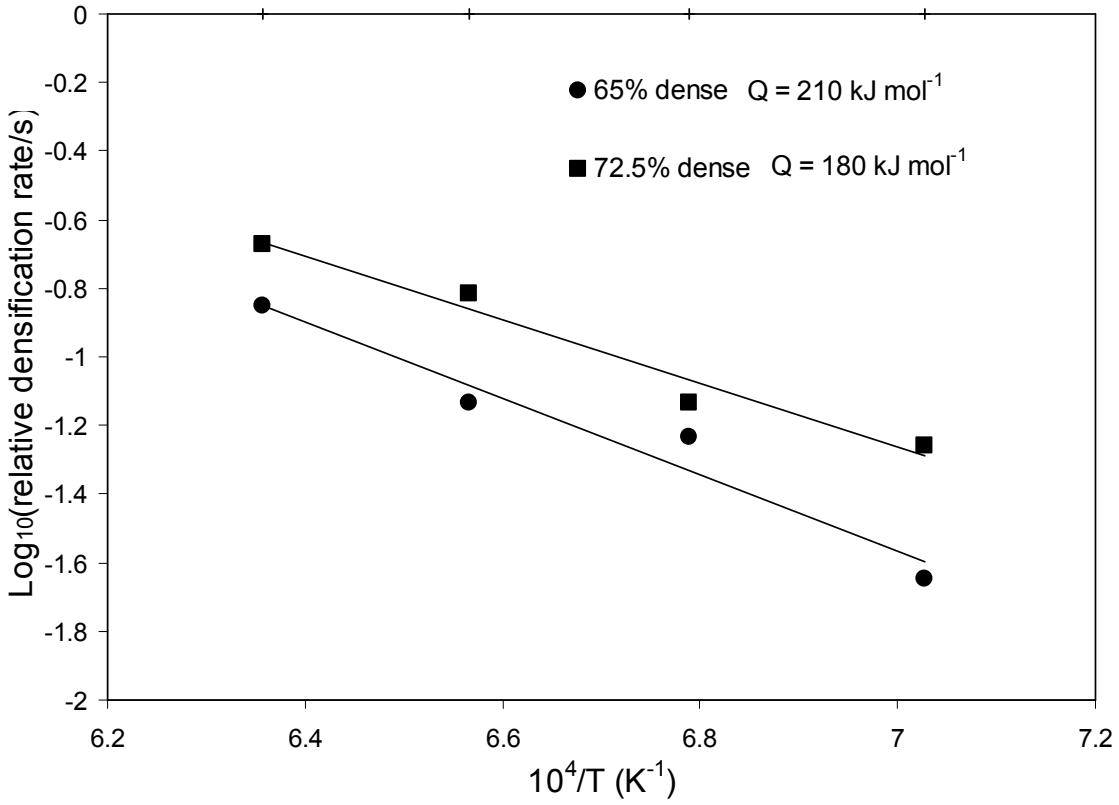

Figure 6 Arrhenius plot of the constrained densification rates at two different densities.

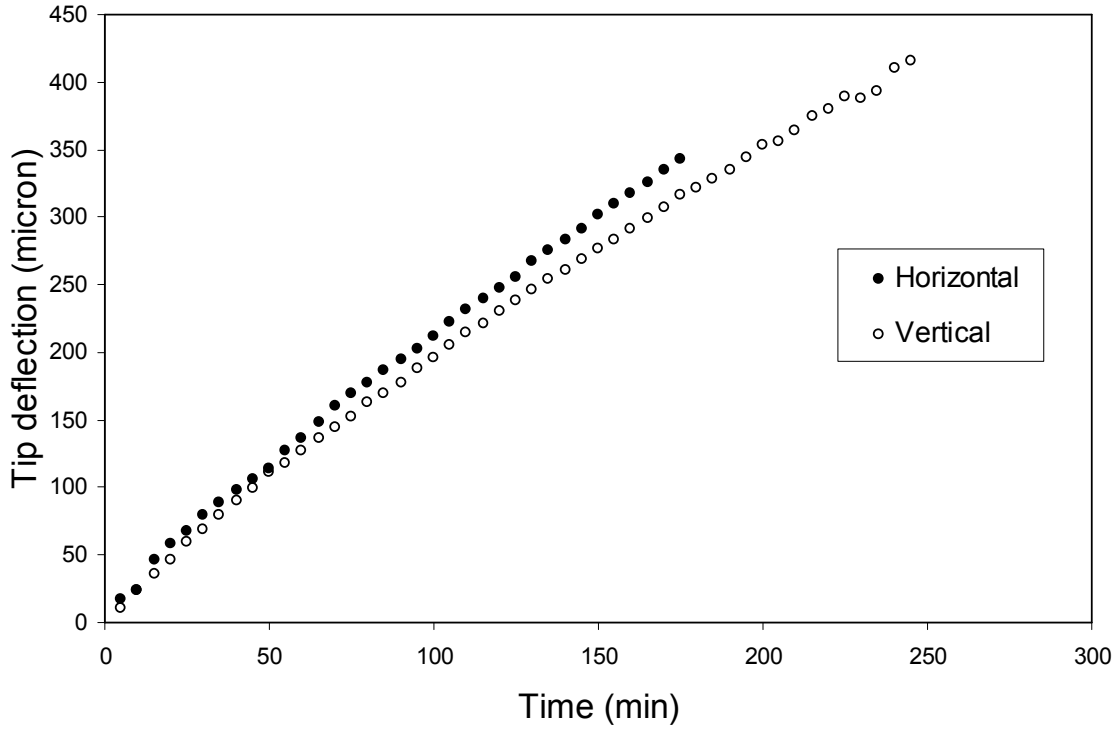

Figure 7 Example of bending of 8YSZ substrate cantilever beams at 1350°C in horizontal (no film) and vertical (with film on one side) orientations. The beam dimensions are 40 mm length by 150 μm thickness.

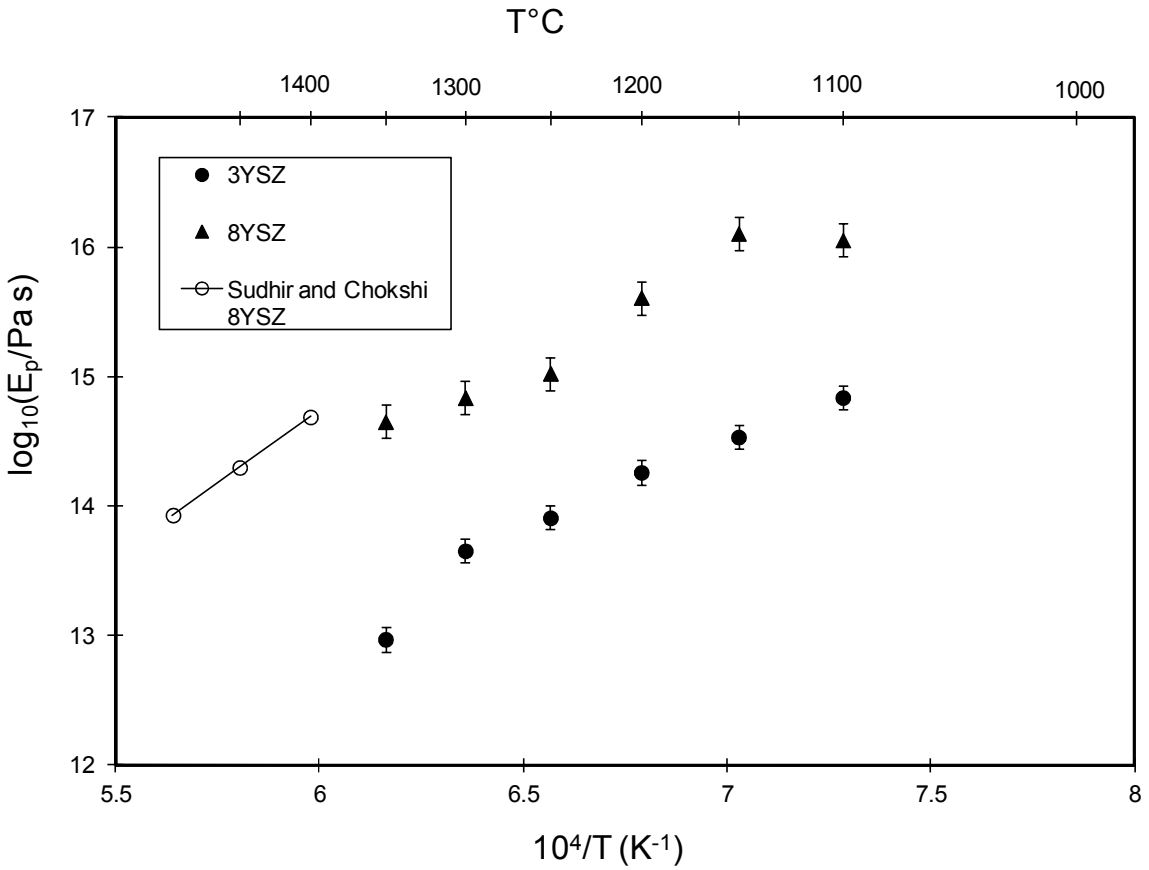

Figure 8 Creep viscosity of dense 3YSZ and 8YSZ substrates used to measure sintering induced stress.

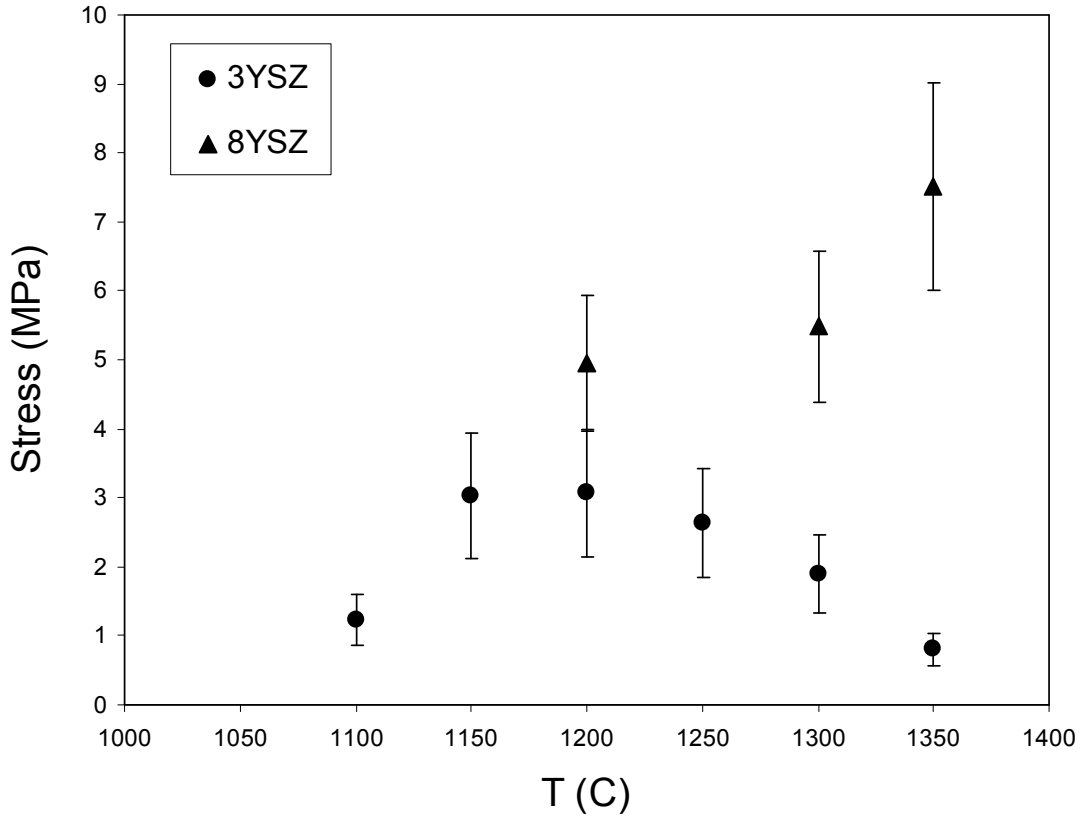

Figure 9 Stress induced during constrained sintering of 3YSZ and 8YSZ films.